

The Bulk-boundary Correspondence in Non-Hermitian Hopf-link Exceptional Line Semimetals

Zhicheng Zhang,^{1,2} Zhesen Yang,^{1,2} and Jiangping Hu^{1,3,4,*}

¹*Beijing National Laboratory for Condensed Matter Physics and Institute of Physics,
Chinese Academy of Sciences, Beijing 100190, China*

²*School of Physical Sciences, University of Chinese Academy of Science, Beijing 100190, China*

³*CAS Center of Excellence in Topological Quantum Computation and Kavli Institute of Theoretical Sciences,
University of Chinese Academy of Sciences, Beijing 100190, China*

⁴*Collaborative Innovation Center of Quantum Matter, Beijing 100871, China*

We consider a 3-dimensional (3D) non-Hermitian exceptional line semimetal model and take open boundary conditions in x, y, and z directions separately. In each case, we calculate the parameter regions where the bulk-boundary correspondence is broken. The breakdown of the bulk-boundary correspondence is manifested by the deviation from unit circles of generalized Brillouin zones (GBZ) and the discrepancy between spectra calculated with open boundary conditions (OBC) and periodic boundary conditions (PBC). The consistency between OBC and PBC spectra can be recovered if the PBC spectra are calculated with GBZs. We use both unit-circle Brillouin zones (BZ) and GBZs to plot the topological phase diagrams. The systematic analysis about the differences between the two phase diagrams suggests that it is necessary to use GBZ to characterize the bulk-boundary correspondence of non-Hermitian models.

I. INTRODUCTION

The Hamiltonians in standard quantum mechanics are required to be Hermitian¹. Over the past two decades, topological properties of Hermitian systems have been studied intensively²⁻⁴, such as topological insulators^{2,5-8}, topological superconductors^{3,9-11} and topological semimetals¹²⁻¹⁵. Non-zero topological invariants always require the existence of corresponding boundary states. This fact is known to be the distinguished bulk-boundary correspondence in Hermitian systems¹⁶.

Recently, the study of topological states has been extended to non-Hermitian systems¹⁷⁻³⁶. Except those with PT symmetry³⁷, the eigenvalues of non-Hermitian Hamiltonians, including open systems³⁸⁻⁴¹, systems with gain and loss⁴²⁻⁶⁴, and interacting electron systems where the self-energy introduced by interactions is treated as non-Hermitian terms^{65,66}, are generally not real. The complex eigenvalues result in novel properties in non-Hermitian systems like exceptional points and enriched topological classifications^{22,67-74}.

One interesting property in non-Hermitian systems is the skin effect^{23,75-79} which states that all the eigenstates with open boundary conditions (OBC) can be localized at one side of the lattice. Unlike the extended Bloch states in Hermitian cases¹⁸, the emergence of these skin modes in non-Hermitian cases indicates the breakdown of the bulk-boundary correspondence. A theorem has been proposed to determine whether there are skin modes and whether the bulk-boundary correspondence of a non-Hermitian system is broken⁸⁰. It claims that the nonzero winding number of periodic boundary conditions (PBC) spectrum ν_E with respect to any reference energy E_b on the complex energy plane requires the existence of skin modes in corresponding OBC system, and vice versa⁸⁰. It has also been suggested that the bulk-boundary corre-

spondence in non-Hermitian systems may be captured by using generalized Brillouin zones (GBZ)s instead of the normal Brillouin zones¹⁸.

In the GBZ approach, recovering the bulk-boundary correspondence is achieved by extending Bloch wave vector k to the complex plane¹⁸. A systematic procedure has been proposed to calculate GBZ numerically^{80,81}. Specifically, the GBZ can be obtained by solving the characteristic equation $\det[H(\beta) - E] = 0$. If $\det[H(\beta) - E]$ is an irreducible algebraic polynomial of E and β , the condition $|\beta_p| = |\beta_{p+1}|$ can lead to the GBZ, where p is the order of the pole of the characteristic equation. On the basis of GBZ, the winding number w is redefined in appendix A. With the redefined winding number, the parameter region corresponding to edge modes can be predicted^{18,81}. More details about this method is attached in Appendix A. Except the numerical method mentioned above, there is an analytic method that can give the explicit expression of GBZs. Algebraic GBZ equation can be translated to a geometric condition by defining auxiliary generalized Brillouin zones (aGBZ)⁸². The aGBZs are calculated analytically with the help of the mathematical concept "resultant". We can obtain the real GBZ from aGBZs with the condition $|\beta_p| = |\beta_{p+1}|$. The details of this analytic method are given in Appendix B.

A non-Hermitian generalization of nodal line semimetal is called exceptional line semimetal, which can exhibit properties absent in the Hermitian case⁸³⁻⁸⁶. For example, topological properties in Hermitian nodal line semimetals are protected by symmetries¹⁴, while non-Hermitian nodal line semimetals are not. The latter also exhibits Hopf-link exceptional lines in certain parameter regions⁸⁷. The bulk-boundary correspondence and the corresponding GBZ approach has been well studied for 1D non-Hermitian models. However, there is not much study about 3D models. Based on these motivations, in this paper we will take OBC in x, y, and z directions separately to study

the bulk-boundary correspondence of 3D non-Hermitian Hopf-link exceptional line semimetals.

The paper is organized as follows. In section II, we introduce the exceptional line semimetal models. In section III, we study the non-Hermitian semimetal model with OBC in z direction. We derive the analytic expression of the GBZs and give the parameter regions where the bulk-boundary correspondence is broken. We manifest the breakdown of the bulk-boundary correspondence by showing the deviation from unit circles of the GBZs and the discrepancy between spectra calculated with OBC and PBC. We also point out that the consistency between OBC and PBC spectra can be recovered if the PBC spectra are calculated with GBZs. Finally, we plot the topological phase diagrams calculated with both unit-circle Brillouin zones (BZs) and GBZs and discuss the reasons for the differences between the two phase diagrams. In section IV and section V, we study similar properties of this model with OBC in y and x directions separately. Finally, we summarize the main results and discuss open problems in section VI.

II. MODEL

First, we consider the following Hermitian model describing nodal line semimetals⁸⁷:

$$H_0(\mathbf{k}) = (\cos k_x + \cos k_y + \cos k_z - m)\sigma_x + \sin k_z \sigma_y, \quad (1)$$

where $m = \frac{21}{8}$. Considering the OBC in z direction, we can write the Hamiltonian as

$$H(k_z) = (\cos k_z + f_0)\sigma_x + \sin k_z \sigma_y, \quad (2)$$

where $f_0 = -m + \cos k_x + \cos k_y$. We diagonalize the Hamiltonian to obtain the PBC energy spectrum and write down the corresponding Hamiltonian in real space to calculate the OBC energy spectrum.

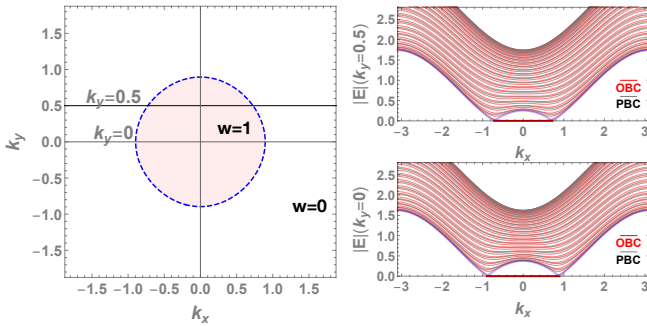


FIG. 1: Bulk-boundary correspondence of Hermitian nodal line semimetal. The left subfigure is the phase diagram, in which the pink region represents topological nontrivial phase ($w = 1$). The right subfigure presents the PBC and OBC spectrum $|E| - k_x$ for $k_y = 0$ and $k_y = 0.5$.

For convenience, we fix $k_y = 0$ and $k_y = 0.5$ to study $|E| - k_x$ relation. Since the Hamiltonian has the chiral

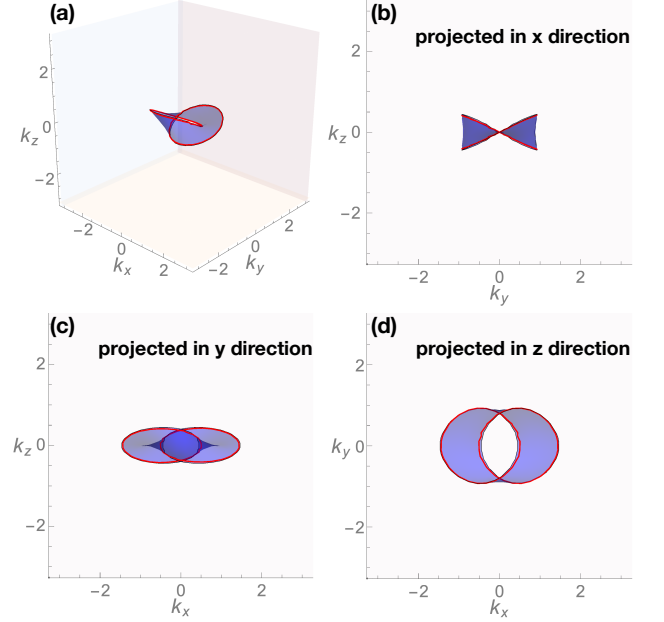


FIG. 2: The Fermi surface of the non-Hermitian exceptional line semimetal model: (a) The Fermi surface is colored in blue. The red lines are its boundaries that form a Hopf link; (b) The projection of the Fermi surface in x direction as two red crossed lines; (c) The projection of the boundary of the Fermi surface in y direction as two closed curves; (d) The projection of the boundary of the Fermi surface in z direction as two closed curves.

symmetry, its eigenvalues have $(E, -E)$ pairs. So we only need to plot the $|E| - k_x$ relation. Shown in Fig. 1, when $k_y = 0$ and $k_y = 0.5$, the PBC spectrum is consistent with OBC spectrum. This shows the bulk-boundary correspondence in this Hermitian model. We also plot the phase diagram, in which the pink region represents topological nontrivial region with the drumhead surface states, and the rest region represents trivial phase. The boundary of the topological nontrivial phase is determined by the gap-closing condition. It is easy to verify that the boundary is: $\cos k_x + \cos k_y = \frac{13}{8}$.

Now we add non-Hermitian terms to the Hermitian nodal line semimetal model to generate non-Hermitian semimetals:

$$H = (\cos k_z - m + \cos k_x + \cos k_y)\sigma_x + \sin k_z \sigma_y + f_x \sigma_x + f_y \sigma_y, \quad (3)$$

where $f_x = \frac{i}{2} \sin k_y$, $f_y = \frac{i}{2} \sin k_x$, and $m = \frac{21}{8}$. We don't add terms that contain σ_z in order to preserve the chiral symmetry.

After diagonalizing the Hamiltonian, we can obtain the eigenvalue equation, i.e. the PBC spectrum

$$E^2 = (\cos k_z - \frac{21}{8} + \cos k_x + \cos k_y + \frac{i}{2} \sin k_y)^2 + (\sin k_z + \frac{i}{2} \sin k_x)^2. \quad (4)$$

By definition, the Fermi surface of this system requires $Re[E(\mathbf{k})] = 0$, which implies $Re[E^2] < 0$ and $Im[E^2] = 0$. Thus, the boundary of Fermi surface is $Re[E^2] = 0$ and $Im[E^2] = 0$. The boundary of the Fermi surface is given by $\sin k_z \sin k_x + (\cos k_z - \frac{21}{8} + \cos k_x + \cos k_y) \sin k_y = 0$ and $(\sin k_z)^2 - \frac{1}{4}(\sin k_x)^2 + (\cos k_z - \frac{21}{8} + \cos k_x + \cos k_y)^2 - (\sin k_y)^2 = 0$, which is shown in Fig. 2(a).

We find that the Fermi surface is a 2D twisting surface. In Fig. 2(a), the Fermi surface is colored in blue. The boundaries of the Fermi surface are two closed curves colored in red, which form the Hopf-link exceptional lines. We project it in x, y, and z directions to fully present the Fermi surface. As is shown in Fig. 2(b), the projection of the Fermi surface boundary in x direction consists of two crossed lines. However, both the projections of Fermi surface boundary in y and z directions are two closed curves, as shown in Fig. 2(c) and Fig. 2(d) separately.

Next we study the bulk-boundary correspondence of the non-Hermitian semimetal model with OBC in z direction, y direction, and x direction one by one.

III. OPEN BOUNDARY IN Z DIRECTION

The Hamiltonian for the non-Hermitian semimetal model with open boundary in z direction is:

$$H(k_z) = (\cos k_z - i \sin k_z + p_{z+}) \frac{\sigma_+}{2} + (\cos k_z + i \sin k_z + p_{z-}) \frac{\sigma_-}{2}, \quad (5)$$

in which $p_{z\pm} = \cos k_x + \cos k_y - m + \frac{i}{2} \sin k_y \pm \frac{1}{2} \sin k_x$, $\sigma_{\pm} = \sigma_x \pm i \sigma_y$, $m = 21/8$. The PBC spectra are given by Eq. (4), where k_x and k_y are variable parameters when we open boundary in z direction. The OBC spectra can be obtained from the eigenvalues of the corresponding Hamiltonian as discussed in Appendix (C).

First, we derive the explicit expression of GBZ and give the parameter region where the bulk-boundary correspondence is broken. Given the matrix form of the real-space Hamiltonian, we can write down the Schrödinger equation in real space: $\psi_{B,n-1} + (f_0 + if_x + f_y)\psi_{B,n} = E\psi_{A,n}$ and $(f_0 + if_x - f_y)\psi_{A,n} + \psi_{A,n+1} = E\psi_{B,n}$. The solution has the form $(\psi_{A,n}, \psi_{B,n}) = \beta_{z,n}(\psi_A, \psi_B)$. The characteristic equation of this model is given by $[(f_0 + if_x + f_y)\beta_z + 1][\beta_z + (f_0 + if_x - f_y)] = E^2\beta_z$. The continuum bands condition requires that $|\beta_{z1}| = |\beta_{z2}|$. Applying Vieta's theorem, we have

$$|\beta_z| = \sqrt{\left| \frac{f_0 + if_x - f_y}{f_0 + if_x + f_y} \right|}. \quad (6)$$

Since $f_y = \frac{1}{2} \sin k_x$, $|\beta_z| = 1$ if and only if $k_x = 0$. Here we don't consider the case where $k_x = \pi$. Thus, the bulk-boundary correspondence is preserved for $k_x = 0$ but broken for $k_x \neq 0$.

Next, we present the breakdown of the bulk-boundary correspondence by showing the deviation from unit circles of the GBZs and the discrepancy between PBC

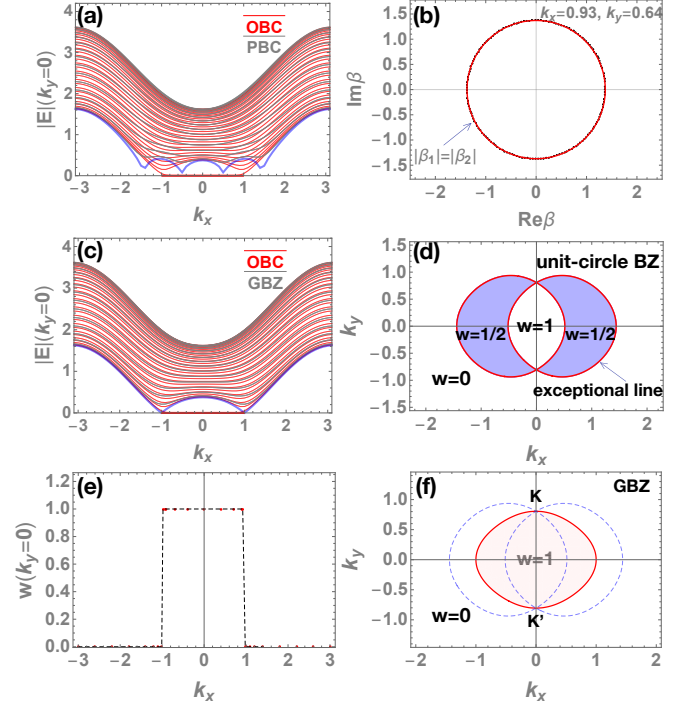


FIG. 3: The non-Hermitian exceptional line semimetal model with open boundary in z direction: (a) the significant differences between PBC and OBC spectra; (b) GBZs calculated with numerical method (black dots) and analytic methods (red circle); (c) the comparison of PBC and OBC spectra ($k_z = 0$). here the PBC spectra are calculated with GBZs; (d) the unit-circle BZ phase diagram calculated with PBC and unit-circle BZ; the winding numbers are labelled in each region; the two red closed curves cross the line $k_y = 0$ at 4 points: $k_x = -1.44, -0.51, 0.51, 1.44$. (e) $w - k_x$ plotted with $k_y = 0$; the range of k_x corresponding to $w = 1$ in Fig. 3(e) is the same as the range of k_x corresponding to zero modes in Fig. 3(c); (f) the GBZ phase diagram with labelled winding number; the pink region corresponds to nontrivial phase with $w = 1$, and the rest region is trivial phase with $w = 0$; the red exceptional line crosses the line $k_y = 0$ at $(-1.00, 0)$ and $(1.00, 0)$; the phase boundaries of unit-circle BZ phase diagram in Fig. 3(d) are drawn as blue dashed lines, which cross the GBZ phase boundary at K and K' points.

spectra and OBC spectra. As an example, we fix $k_x = \arccos 0.6 \approx 0.93$, $k_y = \arccos 0.8 \approx 0.64$ and calculate the OBC spectrum. We choose these parameters because it is convenient to apply the analytic method in Ref.⁸² to calculate GBZ at these parameters. Substituting the OBC spectrum into the characteristic equation and applying the continuum bands condition $|\beta_{z1}| = |\beta_{z2}|$, the trajectory of β_{z1} and β_{z2} leads to the GBZ shown as discrete black dots in Fig. 3(b). The red circle in Fig. 3(b) is the analytic result of GBZ with explicit expression: $(Re\beta_z)^2 + (Im\beta_z)^2 = \sqrt{\frac{4369}{1233}}$. The result is consistent with the numerical one. As we expect, the GBZ is not a unit-circle and the bulk-boundary correspondence is

broken when we take $k_x = 0.93 \neq 0$. Furthermore, we fix $k_y = 0$ and calculate the $|E| - k_x$ relations with PBC and OBC. As shown in Fig. 3(a), when $k_x \neq 0$, there is significant discrepancy between PBC and OBC spectra, implying the existence of the breakdown of bulk-boundary correspondence. However, as shown in Fig. 3(c), if we substitute $e^{ik_z} \rightarrow \beta_z$, the PBC spectra are consistent with the OBC spectra. Namely, the introduction of GBZ recovers the bulk-boundary correspondence in this non-Hermitian model.

We then calculate the topological phase diagrams. When we use a unit-circle Brillouin zone, the gap closing condition $|E| = 0$ of Eq. (4) requires both the real part and imaginary part of E to be 0, leading to two equations: $\cos k_z + f_0 \mp f_y = 0$ and $f_x \pm \sin k_z = 0$. The two equations together give rise to $f_x^2 + (f_0 \mp f_y)^2 = 1$, which are the red exceptional lines shown in Fig. 3(d). To specify the topological property of the rest region in $k_x - k_y$ plane, we calculate winding numbers and label them in each region. The unit-circle BZ phase diagram is the same as the projection of the Fermi surface in z direction shown in Fig. 2(d). This is easy to understand, because both the two diagrams are calculated with PBC and unit-circle BZs. To calculate the GBZ phase diagram, we substitute e^{ik_z} with β_z into Eq. (4). The gap-closing condition gives rise to $(f_0^2 + f_x^2 - f_y^2)^2 + 4f_x^2 f_y^2 = 1$, as shown in Fig. 3(f) where the topological nontrivial and trivial phases are indicated in the pink and white regions respectively. To compare the two phase diagrams, the phase boundaries of unit-circle BZ phase diagram in Fig. 3(d) are drawn as blue dashed curves in Fig. 3(f), which intersect with the GBZ phase boundary at K and K' points. Fig. 3(e) shows the $w - k_x$ relation with $k_y = 0$. The range of k_x corresponding to $w = 1$ in Fig. 3(e) is consistent with the range of k_x for zero modes of OBC spectrum in Fig. 3(c). Thus, we can conclude that GBZ phase diagram gives the correct bulk-boundary correspondence.

Next, we explain the differences between the phase boundaries of the two phase diagrams. The phase boundaries in both two phase diagrams are calculated from the gap-closing condition of the characteristic equation:

$$E^2 = \left(\frac{1}{2}(\beta_z + \frac{1}{\beta_z}) - m + \cos k_x + \cos k_y + \frac{i}{2} \sin k_y\right)^2 + \left(\frac{1}{2i}(\beta_z - \frac{1}{\beta_z}) + \frac{i}{2} \sin k_x\right)^2. \quad (7)$$

The difference is that the constraint $|\beta_z| = 1$ is applied to calculate the phase boundary in unit-circle BZ phase diagram while the constraint $|\beta_{z1}| = |\beta_{z2}|$ is applied to obtain the phase boundary in GBZ phase diagram. When we take $|\beta_z| = 1$, the characteristic equation becomes Eq. (4). This characteristic equation leads to the unit-circle BZ phase diagram. However, when we take $|\beta_{z1}| = |\beta_{z2}|$, the gap-closing condition of the characteristic equation leads to $|\beta_z| = \sqrt{|\frac{f_0 + if_x - f_y}{f_0 + if_x + f_y}|}$. In general, we don't have $|\beta_z| = 1$. This is the origin of the differences between the phase boundaries of the two phase diagrams. However, if

the constraint $|\beta_{z1}| = |\beta_{z2}|$ leads to $|\beta_{z1}| = |\beta_{z2}| = 1$ at some parameters, the characteristic equation will also be Eq. (4). It means that the phase boundaries of unit-circle BZ phase diagram and GBZ phase diagram will intersect at these parameters. In our model, as $|\beta_z| = \sqrt{|\frac{f_0 + if_x - f_y}{f_0 + if_x + f_y}|}$ and $f_y = \frac{1}{2} \sin k_x$, the phase boundaries of the two phase diagrams will intersect at points where $k_x = 0$. This is clearly shown in Fig. 3(f), where the two phase boundaries cross at K and K' points on the line $k_x = 0$.

We may also notice that there exists $\omega = 1/2$ region in the unit-circle BZ phase diagram Fig. 3(d). The $\omega = 1/2$ region vanishes in the GBZ phase diagram Fig. 3(f). According to appendix A, for a two band model $H = R_+(\beta)\sigma_+ + R_-(\beta)\sigma_-$ with chiral symmetry, the definition of the eigenstate winding number is $\omega = (\omega_+ - \omega_-)/2$. ω_+ is the winding number of $R_+(\beta)$, and ω_- is the winding number of $R_-(\beta)$ when β goes along the GBZ C_β . We can get $\omega = 1/2$ if we choose proper parameters. When we take OBC in z direction of our model Eq. (1) and take the parameters $k_x = 1.0$ and $k_y = 0.2$ in Eq. (4), we have $\omega_+ = 1$ and $\omega_- = 0$, giving rise to $\omega = 1/2$. For non-Hermitian systems, we can also define the eigenvalue winding number: $\omega_E = (\omega_+ + \omega_-)/2$. As is shown in Ref.⁸⁰, for OBC spectra and GBZ spectra, we have $\omega_E = 0$, indicating that $\omega_+ = -\omega_-$. Thus, $\omega_S = (\omega_+ - \omega_-)/2 \in \mathcal{Z}$, and the $\omega_S = 1/2$ region will vanish in GBZ phase diagram.

IV. OPEN BOUNDARY IN Y DIRECTION

The Hamiltonian for the non-Hermitian semimetal model with open boundary in y direction is:

$$H(k_y) = (\cos k_y + \frac{i}{2} \sin k_y + p_{y+}) \frac{\sigma_+}{2} + (\cos k_y + \frac{i}{2} \sin k_y + p_{y-}) \frac{\sigma_-}{2}, \quad (8)$$

in which $p_{y\pm} = \cos k_x + \cos k_z - m \mp i \sin k_z \pm \frac{1}{2} \sin k_x$, $m = \frac{21}{8}$. The PBC spectra are given by Eq. (4), where k_x and k_z are variable parameters when we open boundary in y direction. Besides, we can obtain OBC spectrum by diagonalizing the corresponding real-space Hamiltonian shown in Appendix(C2).

First, we derive the expression of GBZs and determine the parameter region where the bulk-boundary correspondence is broken. To calculate the GBZs, we substitute e^{ik_y} in Eq. (4) with β_y and write down the characteristic equation:

$$E^2 = (\frac{3}{4}\beta_y + t_1 + \frac{1}{4\beta_y})^2 + t_2^2, \quad (9)$$

where $t_1 = \cos k_z - m + \cos k_x$, $t_2 = \sin k_z + \frac{i}{2} \sin k_x$, and $m = \frac{21}{8}$. t_1 and t_2 are independent of β_y . Then according to Vieta's theorem, the 4 solutions have the relation $|\beta_a||\beta_b| = \frac{1}{3}$ and $|\beta_c||\beta_d| = \frac{1}{3}$. Thus, the continuum band

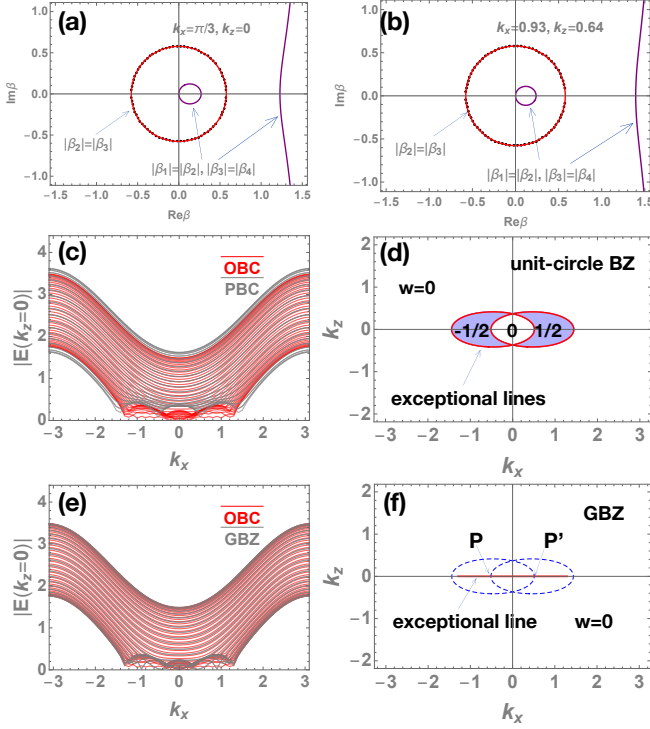


FIG. 4: The non-Hermitian nodal line semimetal model with open boundary in y direction: (a) the circle GBZ with $r = \frac{1}{\sqrt{3}}$ when we take $k_x = \frac{\pi}{3}, k_z = 0$; (b) the circle GBZ with $r = \frac{1}{\sqrt{3}}$ when we take $k_x = 0.93, k_z = 0.64$; (c) the discrepancy between PBC and OBC spectra with $k_z = 0$ implies that the bulk-boundary correspondence is broken; (d) the boundaries of the PBC phase diagram are two red exceptional lines, intersecting the line $k_z = 0$ at $k_x = -1.44, -0.51, 0.51, 1.44$; (e) the OBC spectrum is consistent with PBC spectrum calculated with GBZ; (f) the phase diagram calculated with GBZ; the red line $k_z = 0, k_x \in (-1.29, 1.29)$ is the exceptional line, and the rest region corresponds to the topological trivial phase; the blue dashed lines are the phase boundaries of the unit-circle BZ phase diagram in Fig. 4(d), intersecting the red exceptional line at P and P'.

condition $|\beta_{y2}| = |\beta_{y3}|$ requires that $|\beta_{y2}| = |\beta_{y3}| = \frac{1}{\sqrt{3}}$. It means that the GBZ is a circle with $r = \frac{1}{\sqrt{3}} \approx 0.577$, which is independent of k_x and k_z . We then conclude that the bulk boundary correspondence is broken in this case for any parameters in $k_x - k_z$ plane.

Next, we manifest the breakdown of the bulk-boundary correspondence by showing the deviation from unit circles of GBZs and the significant differences between PBC and OBC spectra. For example, we calculate the OBC spectra with parameters $k_x = \frac{\pi}{3}, k_z = 0$, and substitute the spectra into the characteristic equation Eq. (9). The condition $|\beta_{y2}| = |\beta_{y3}|$ leads to numerical GBZ shown as black dots in Fig. 4(a). The analytic method in Ref.⁸² also gives a GBZ. The analytic expression of the GBZ is $x^2 + y^2 = \frac{1}{3}$, which is plotted as a red circle in Fig. 4(a). It is consistent with the numerical result shown in

Fig. 4(a). When we take $k_x = 0.93, k_z = 0.64$, we will obtain the circle GBZ with $r = \frac{1}{\sqrt{3}}$ shown in Fig. 4(b). These results support the fact that the bulk-boundary correspondence is broken for any parameters in the $k_x - k_z$ plane. To compare the PBC and OBC spectra, we study the $|E| - k_x$ relation for $k_z = 0$. The result is shown in Fig. 4(c). The PBC spectra are quite different from OBC ones, indicating the breakdown of bulk-boundary correspondence. However, if we apply the transformation $e^{ik_y} \rightarrow \beta_y = \frac{1}{\sqrt{3}}e^{i\theta}$, the PBC spectra become $E^2 = (\cos k_z - 21/8 + \cos k_x + \frac{\sqrt{3}}{2} \cos \theta)^2 + (\sin k_z + i \sin k_x/2)^2$. The comparison between the OBC spectra and the new PBC spectra calculated with GBZ is shown in Fig. 4(e). Obviously, the introduction of GBZ in the calculation of PBC spectra recovers the consistency between the PBC and OBC spectra.

The topological phase diagrams can be calculated by applying the gap-closing condition. To obtain the unit-circle BZ phase diagram, we assume that $|\beta_y| = 1$. The gap closing condition of PBC spectra Eq. (4) gives red exceptional lines in Fig. 4(d): $4(\sin k_z)^2 + (\cos k_x \pm \frac{1}{2} \sin k_x + \cos k_z - \frac{21}{8})^2 = 1$. The winding numbers are labelled in each region in Fig. 4(d). This phase diagram shows little difference from the projection of Fermi surface in y direction Fig. 2(c). To get the GBZ topological phase diagram, we substitute e^{ik_y} with $\frac{1}{\sqrt{3}}e^{i\theta}$ in Eq. (4), the gap closing condition leads to the phase diagram shown in Fig. 4(f). The parameter region for the red exceptional line is $k_z = 0, k_x \in (-1.29, 1.29)$, and the rest region represents topological trivial phase. To show the difference between the two phase diagrams, the phase boundary of the unit-circle BZ phase diagram is shown as blue dashed curves in Fig. 4(f), which intersect with the red exceptional line of GBZ phase diagram at P and P' points.

We then analyze the differences between the phase boundaries of the two phase diagrams. The phase boundaries of both the two phase diagrams are calculated with the gap-closing condition of the characteristic equation Eq. (9). To determine the phase boundary of the GBZ phase diagram, we use the constraint $|\beta_{y2}| = |\beta_{y3}|$ to solve the characteristic equation with $E = 0$. The result is $|\beta_{y2}| = |\beta_{y3}| = \frac{1}{\sqrt{3}} \neq 1$. Thus, we expect that GBZ phase boundary is different from unit-circle BZ phase diagram. However, we notice that the phase boundaries of the two phase diagrams intersect at P and P' points. In open boundary in z direction case, the characteristic equation is a quadratic equation. $|\beta_{z1}| = |\beta_{z2}| = 1$ leads to the intersecting between the phase boundaries of the two phase diagrams, and vice versa. When there is intersecting between the two phase boundaries at some points, we have $|\beta_{z1}| = |\beta_{z2}|$, and at least one of the solutions satisfy $|\beta_z| = 1$, leading to $|\beta_{z1}| = |\beta_{z2}| = 1$. Nonetheless, it is not the case when we open boundary in y direction. The characteristic equation Eq. (9) is a quartic equation. $|\beta_{y2}| = |\beta_{y3}| = 1$ still leads to the intersecting between the phase boundaries of the two phase diagrams. However, because the characteristic

equation has four solutions, at the intersecting points the two conditions $|\beta_{y2}| = |\beta_{y3}|$ and the existence of solution satisfying $|\beta_y| = 1$ do not necessarily lead to $|\beta_{y2}| = |\beta_{y3}| = 1$. In fact, at P' point $(k_x, k_z) = (0.514, 0)$ the characteristic equation Eq. (9) with $E = 0$ gives solutions: $\beta_1 = 1, \beta_2 = 0.34 + i0.47, \beta_3 = 0.34 - i0.47, \beta_4 = \frac{1}{3}$ and $|\beta_1| = 1, |\beta_2| = \frac{1}{\sqrt{3}}, |\beta_3| = \frac{1}{\sqrt{3}}, |\beta_4| = \frac{1}{3}$. At the intersecting point P' the condition $|\beta_{y2}| = |\beta_{y3}|$ is satisfied by the second and third solution, while $|\beta_{y1}| = 1$ is satisfied by the first solution. This is the reason why the two phase boundaries intersect at P and P' points even if at the two points we have $|\beta_{y2}| = |\beta_{y3}| \neq 1$.

We find that there is a significant difference between y and z open boundary cases. The exceptional line in the GBZ phase diagram in z open boundary case encloses finite area, while the exceptional line in the GBZ phase diagram in y open boundary case is an open arc with zero area. In fact, the behavior of exceptional lines and Fermi surfaces is highly dependent of the concrete property of the non-Hermitian models. When we take open boundary condition in z direction, we get 1D model Eq. (5). We can calculate the OBC spectrum, finding that there are zero modes. The parameter region corresponding to zero modes is consistent with $\omega = 1$ region in GBZ phase diagram Fig. 3(f). Thus, the exceptional line changes from two intersecting closed curves in unit-circle BZ phase diagram into a closed curve enclosing topological nontrivial region in GBZ phase diagram. We also open boundary in y direction to get 1D model Eq. (8) and calculate the OBC spectrum. However, we cannot find zero modes corresponding to topological nontrivial states. Thus, different from z open boundary case, the exceptional line in y open boundary case collapses into an open arc and doesn't enclose topological nontrivial region with finite area.

V. OPEN BOUNDARY IN X DIRECTION

The Hamiltonian of the non-Hermitian exceptional line semimetal model with OBC in x direction is:

$$H(k_x) = (\cos k_x + \frac{1}{2} \sin k_x + p_{x+}) \frac{\sigma_+}{2} + (\cos k_x - \frac{1}{2} \sin k_x + p_{x-}) \frac{\sigma_-}{2}, \quad (10)$$

in which $p_{x\pm} = \cos k_y + \cos k_z - m + \frac{i}{2} \sin k_y \mp i \sin k_z$, and $m = \frac{21}{8}$. The PBC spectra are given by Eq. (4), where k_y and k_z are variable parameters when we open boundary in x direction. OBC spectra are calculated from the corresponding real-space OBC Hamiltonians in Appendix (C3).

First, we calculate the GBZs and give the parameter region where the bulk-boundary correspondence is broken. To calculate GBZs, we substitute e^{ik_x} with β_x in Eq. (4)

to obtain the characteristic equation:

$$E^2 = (\frac{1}{2}(\beta_x + \frac{1}{\beta_x}) + \cos k_z - 21/8 + \cos k_y + \frac{i}{2} \sin k_y)^2 + (\frac{1}{4}(\beta_x - \frac{1}{\beta_x}) + \sin k_z)^2, \quad (11)$$

The structure of this characteristic equation is more complex than the above two cases with open boundary in z and y directions. But we can still get the analytic expression of GBZs when we take $k_z = 0$. With $k_z = 0$, the characteristic equation Eq. (11) is invariant under the transformation $\beta_x \rightarrow \frac{1}{\beta_x}$. Thus, if β_x is a solution of the equation, $\frac{1}{\beta_x}$ is also a solution. Without loss of generality, we suppose that there are four solutions to the equation: $\beta_1, \beta_2, \frac{1}{\beta_1}, \frac{1}{\beta_2}$, and $|\beta_1| \leq |\beta_2| \leq 1$. The ordering of the moduli of β s is $|\beta_1| \leq |\beta_2| \leq |\frac{1}{\beta_2}| \leq |\frac{1}{\beta_1}|$. Thus, the continuum band condition $|\beta_2| = |\beta_3|$ requires that $|\beta_2| = |\frac{1}{\beta_2}| = 1$. Thus, the Brillouin zone is a unit circle if $k_z = 0$. There is no analytic expression of GBZ if $k_z \neq 0$. However, we can use the theorem in Ref.⁸⁰ to verify whether the bulk-boundary correspondence is broken. We find that for $k_z = 0$ the PBC spectra in $ReE - ImE$ plane have winding number $\nu_E = 0$ with respect to any reference point in the complex energy plane, while for $k_z \neq 0$ all the PBC spectra have winding number $\nu_E \neq 0$. According to the theorem in Ref.⁸⁰, we can conclude that the bulk-boundary correspondence is preserved for $k_z = 0$ but broken for $k_z \neq 0$.

Next, we show the breakdown of the bulk-boundary correspondence by GBZs and the discrepancy between PBC and OBC spectra. We take $k_y = 0.93$ and $k_z = 0$ and calculate the OBC spectrum. Substituting the spectrum into the characteristic equation Eq. (11), the continuum band condition $|\beta_{x2}| = |\beta_{x3}|$ leads to a unit circle GBZ as shown in Fig. 5(a). We also take $k_y = 0.93, k_z = 0.64$. The corresponding GBZ is not a unit circle as shown in Fig. 5(b). The two results are consistent with the previous conclusion that the GBZ is a unit circle if $k_z = 0$ but is not a unit circle if $k_z \neq 0$. Then we study the $|E| - k_y$ relation with $k_z = 0.35$. As is shown in Fig. 5(c), the differences between PBC and OBC spectra show the breakdown of the bulk-boundary correspondence for $k_z \neq 0$.

Then we calculate the topological phase diagrams. To calculate the unit-circle BZ phase diagram, we assume that the Brillouin zone is a unit circle. The gap-closing condition leads to $\cos k_y + \cos k_z > 1.51$ and $\sin k_z = \pm \frac{1}{2} \sin k_y$, which are two red exceptional lines shown in Fig. 5(d). The rest region is trivial phase with $w = 0$. This phase diagram is the same as the projection of Fermi surface in x direction shown in Fig. 2(b). Furthermore, we calculate the GBZ phase diagram. The gap-closing condition of the characteristic equation Eq. (11) and continuum band condition $|\beta_{x2}| = |\beta_{x3}|$ also lead to $\cos k_y + \cos k_z > 1.51$ and $\sin k_z = \pm \frac{1}{2} \sin k_y$. The GBZ phase diagram is shown in Fig. 5(f). To compare the two phase diagrams, we plot the exceptional lines of

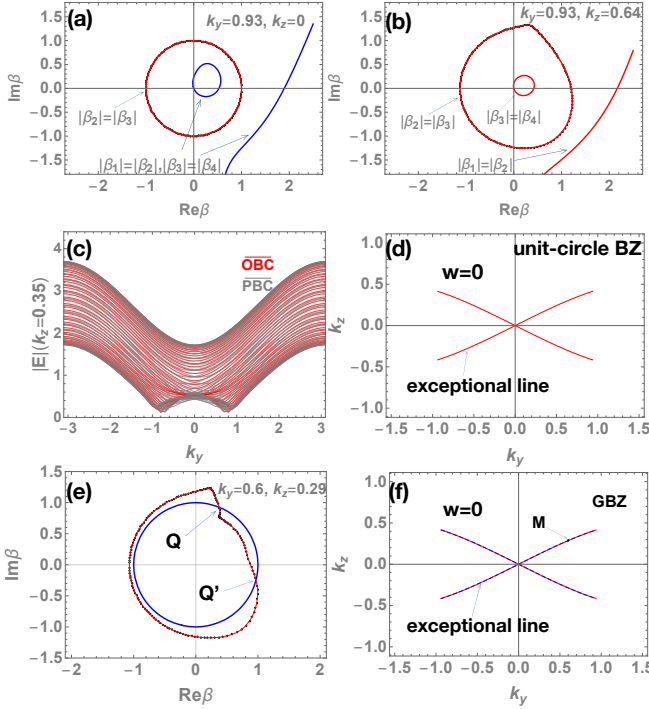


FIG. 5: The non-Hermitian nodal line semimetal model with open boundary in x direction: (a) the unit circle GBZ with $k_y = 0.93, k_z = 0$ from both numerical results (black dots) and analytic results (red closed lines); (b) the GBZ with $k_y = 0.93, k_z = 0.64$, which is not a unit circle. (c) the comparison between the PBC and OBC spectra with $k_z = 0.35$; (d) the unit-circle BZ topological phase diagram with the end points of the exceptional lines at $(k_x, k_y) = (\pm 0.94, \pm 0.41)$; (e) GBZ for M point $(k_y, k_z) = (0.6, 0.29)$ in which the black dots are numerical results; red lines connect these numerical dots to show the GBZ more clearly; the blue curve is a unit circle that intersect the GBZ at Q and Q' points; (f) shows the GBZ phase diagram in which the red lines are the exceptional lines; the dashed blue lines are the exceptional lines of the unit-circle BZ phase diagram.

unit-circle BZ phase diagram as blue dashed lines. We find that the two exceptional lines totally overlap and the two phase diagrams are exactly the same.

Finally, we explain the reasons why the two phase diagrams are identical. Both the two exceptional lines are determined by the gap-closing condition of the characteristic equation Eq. (11). To obtain the exceptional lines in the GBZ phase diagram, we apply the constraint $|\beta_{x2}| = |\beta_{x3}|$. Then the characteristic equation Eq. (11) with $E = 0$ gives rise to $|\beta_{x2}| = |\beta_{x3}| = 1$, which is independent of k_y and k_z . This explains why the two phase diagrams are exactly the same. To understand why we have $|\beta_{x2}| = |\beta_{x3}| = 1$ even if $k_z \neq 0$ and the bulk-boundary correspondence is broken, we choose the M point $(0.6, 0.29)$ in Fig. 5(f) on the exceptional line as an example. To get the GBZ of M point, we fix $k_y = 0.6, k_z = 0.29$ and calculate the OBC spectra from

the real-space Hamiltonian in Appendix (C3). Substituting the spectra into the characteristic equation Eq. (11), the continuum bands condition $|\beta_{x2}| = |\beta_{x3}|$ leads to the GBZ shown as black dots in Fig. 5(e). The red lines connect these black dots to present the GBZ more clearly. The GBZ is not a unit circle as we expect. On the other hand, when we use gap-closing condition $E = 0$ and the continuum band condition $|\beta_{x2}| = |\beta_{x3}|$ to solve the characteristic equation, we have $\beta_1 = 0.49 + i0.22, \beta_2 = 0.38 + i0.93, \beta_3 = 0.97 - i0.25, \beta_4 = 0.40 - i1.80$ and $|\beta_1| = 0.54, |\beta_2| = |\beta_3| = 1, |\beta_4| = 1.84$. β_2 and β_3 are plotted in Fig. 5(e) as Q and Q' points, which are exactly the crossing points of the GBZ and the unit circle. It means that although the GBZ of M point is not a unit circle, it crosses the unit circle at Q and Q' points, which correspond to the eigenenergy $E = 0$ in the OBC spectrum. This example suggests that it is necessary to introduce GBZ to characterize the bulk-boundary correspondence. Because even if the unit-circle BZ phase diagram is the same as GBZ phase diagram, the bulk-boundary correspondence is broken for $k_z \neq 0$, which can be clearly shown by the deviation from unit circles of GBZs.

VI. SUMMARY AND DISCUSSIONS

In summary, we study a non-Hermitian exceptional line semimetal model with open boundary in z, y, and x directions separately. In each case, we calculate the parameter region corresponding to the breakdown of the bulk-boundary correspondence. The GBZs and the discrepancy between PBC and OBC spectra present the breakdown of the bulk-boundary correspondence.

We demonstrate that in all considered cases, the numerical method and analytic method result in the same GBZs. The PBC spectrum calculated with GBZ is consistent with the OBC spectrum. Namely, the introduction of GBZ recovers the bulk-boundary correspondence in these models. Both unit-circle BZ phase diagrams and GBZ phase diagrams are plotted. The difference between the unit-circle BZ phase diagrams and GBZ phase diagrams highlights the significance of GBZ in characterizing the bulk-boundary correspondence of non-Hermitian models.

As is shown in this article, the aforementioned methods to calculate GBZs work well when we open boundary in one direction. However, a systematic method to calculate the GBZs of non-Hermitian models with open boundary in two or more directions hasn't yet been proposed up to now. In future, we hope to find a generalized method to calculate GBZ and define topological invariants for non-Hermitian models with open boundaries in two and more directions.

ACKNOWLEDGEMENTS

We thank Kai Zhang sincerely for his helpful suggestions. Jiangping Hu is supported by the Ministry of Science and Technology of China 973 program (Grant No. 2017YFA0303100), National Science Foundation of China (Grant No. NSFC-11888101), and the Strategic Priority Research Program of CAS (Grant No. XDB28000000).

Appendix A: Numerical Method to Calculate GBZ

For a given model with chiral symmetry, we first write it as a Bloch Hamiltonian $H(k)$, then we get $H(\beta)$ through the transformation $e^{ik} \rightarrow \beta$. Next we solve the characteristic equation $\det[H(\beta) - E] = 0$. Supposing that there are $2M$ degrees of freedom in this equation for given E , we can get $2M$ solutions:

$$|\beta_1| \leq |\beta_2| \leq \dots \leq |\beta_{2M}|. \quad (A1)$$

In principle, E and GBZ can be got through the condition $|\beta_M| = |\beta_{M+1}|$ ^[81]. We calculate OBC spectrum and get eigenvalues E s for given parameters. Then we can substitute E s into the characteristic equation $\det[H(\beta) - E] = 0$ and get $2M$ solutions β s. GBZ C_β is given by the condition: $|\beta_M| = |\beta_{M+1}|$.

The definition of winding number is also put forward for non-Hermitian systems: $w = \frac{i}{2\pi} \int_{C_\beta} \text{Tr}[q^{-1}(\beta)dq]$, where C_β is the GBZ, and q is a submatrix of Q matrix^[81]. In particular, for a two band model:

$$\mathcal{H}_\beta = R_+(\beta)\sigma_+ + R_-(\beta)\sigma_- = \begin{pmatrix} 0 & R_+(\beta) \\ R_-(\beta) & 0 \end{pmatrix}, \quad (A2)$$

the winding number is defined^[81] as

$$w = -\frac{1}{2\pi} \frac{[\arg R_+(\beta) - \arg R_-(\beta)]_{C_\beta}}{2}. \quad (A3)$$

In this definition, the winding number is $\omega = (\omega_+ - \omega_-)/2$ with $\omega_+ = -[\arg R_+(\beta)]_{C_\beta}/(2\pi)$, $\omega_- = -[\arg R_-(\beta)]_{C_\beta}/(2\pi)$. The solutions of the characteristic equation β s form the GBZ, which is a closed curve C_β . $R_+(\beta)$ and $R_-(\beta)$ map β to two closed curves, having winding numbers ω_+ and ω_- separately.

Appendix B: Analytic Method to Calculate GBZ

Ref.^[82] makes use of the mathematical tool resultant to get so-called auxiliary generalized Brillouin zone (aGBZ). GBZ can be extracted from aGBZs. Let's consider a model with characteristic equation $f(\beta, E) = 0$. Supposing that the highest order of the poles of the characteristic equation is p , the condition for GBZ is $|\beta_p| = |\beta_{p+1}|$. But the direct application of this condition is intractable. Thus, we relax

the condition to be $|\beta_j| = |\beta_{j+1}|$, so the requirement for GBZ becomes $f(\beta, E) = f(\beta e^{i\theta}, E) = 0$.

Obviously, there are 5 variables $\beta_x, \beta_y, E_x, E_y, \theta$ (β_x represents $\text{Re}\beta$ while β_y represents $\text{Im}\beta$; E_x represents $\text{Re}E$ while E_y represents $\text{Im}E$). We know that the Brillouin zone is an equation that contains only β_x and β_y , thus we need eliminate E_x, E_y, θ . First we calculate the resultant $R^{f, f^\theta}(\beta)$ to eliminate E , which is the resultant between $f(\beta, E)$ and $f^\theta(\beta, E)$. To eliminate θ , we need to calculate the resultant (we denote it as $F_\alpha(\beta_x, \beta_y)$) between the real part and imaginary part of $R^{f, f^\theta}(\beta)$. Finally, the algebraic equation

$$F_\alpha(\beta_x, \beta_y) = 0. \quad (B1)$$

gives aGBZs, and we can then apply the condition $|\beta_p| = |\beta_{p+1}|$ to get real GBZs. It is noteworthy that this method can give the analytic expression for GBZs, so we needn't consider the lattice size or suffer from numerical errors.

Appendix C: The OBC Real-space Hamiltonians

The model with OBC in z direction: under the basis $\Psi = (C_{A1}, C_{B1}, C_{A2}, C_{B2}, C_{A3}, C_{B3}, \dots)^T$ where C_{Ai}^\dagger creates an electron on the A site of i th unit cell in z direction, the real-space Hamiltonian in matrix form is:

$$\begin{pmatrix} 0 & f_0 + if_x + f_y & 0 & \dots \\ f_0 + if_x - f_y & 0 & 1 & \dots \\ 0 & 1 & 0 & \dots \\ \dots & \dots & \dots & \ddots \end{pmatrix}, \quad (C1)$$

where $f_0 = \cos k_x + \cos k_y - m$, $f_x = \frac{1}{2} \sin k_y$, $f_y = \frac{1}{2} \sin k_x$, and $m = \frac{21}{8}$.

The model with OBC in y direction: under the basis $\Psi = (C_{A1}, C_{B1}, C_{A2}, C_{B2}, C_{A3}, \dots)^T$ where C_{Ai}^\dagger creates an electron on the A site of i th unit cell in y direction, the corresponding Hamiltonian in real space is:

$$\begin{pmatrix} 0 & q_{1y} + q_{2y} & 0 & \dots \\ q_{1y} - q_{2y} & 0 & \frac{1}{2} + \frac{i}{4} & \dots \\ 0 & \frac{1}{2} - \frac{i}{4} & 0 & \dots \\ \dots & \dots & \dots & \ddots \end{pmatrix}, \quad (C2)$$

where $q_{1y} = \cos k_x + \cos k_z - m$, $q_{2y} = -i \sin k_z + \frac{1}{2} \sin k_x$, and $m = \frac{21}{8}$.

The model with OBC in x direction: with the basis $\Psi = (C_{A1}, C_{B1}, C_{A2}, C_{B2}, C_{A3}, \dots)^T$ where C_{Ai}^\dagger creates an electron on the A site of i th unit cell in x direction, the corresponding real-space Hamiltonian in matrix form is:

$$\begin{pmatrix} 0 & q_{1x} + q_{2x} & 0 & \frac{1}{2} - \frac{i}{4} & \dots \\ q_{1x} - q_{2x} & 0 & \frac{1}{2} + \frac{i}{4} & 0 & \dots \\ 0 & \frac{1}{2} + \frac{i}{4} & 0 & q_{1x} + q_{2x} & \dots \\ \frac{1}{2} - \frac{i}{4} & 0 & q_{1x} - q_{2x} & 0 & \dots \\ \dots & \dots & \dots & \dots & \ddots \end{pmatrix}, \quad (C3)$$

where $q_{1x} = \cos k_z - m + \cos k_y + \frac{i}{2} \sin k_y$, $q_{2x} = -i \sin k_z$, and $m = \frac{21}{8}$.

-
- * Electronic address: jphu@iphy.ac.cn
- ¹ J. J. Sakurai, J. Napolitano, *et al.*, *Modern quantum mechanics*, Vol. 185 (Pearson, Harlow, 2014).
 - ² M. Z. Hasan and C. L. Kane, *Rev. Mod. Phys.* **82**, 3045 (2010).
 - ³ X.-L. Qi and S.-C. Zhang, *Rev. Mod. Phys.* **83**, 1057 (2011).
 - ⁴ J. E. Moore, *Nature* **464**, 194 (2010).
 - ⁵ L. Fu, C. L. Kane, and E. J. Mele, *Phys. Rev. Lett.* **98**, 106803 (2007).
 - ⁶ L. Fu and C. L. Kane, *Phys. Rev. B* **76**, 045302 (2007).
 - ⁷ C.-X. Liu, X.-L. Qi, H. Zhang, X. Dai, Z. Fang, and S.-C. Zhang, *Phys. Rev. B* **82**, 045122 (2010).
 - ⁸ H. Zhang, C.-X. Liu, X.-L. Qi, X. Dai, Z. Fang, and S.-C. Zhang, *Nature Physics* **5**, 438 (2009).
 - ⁹ A. P. Schnyder, S. Ryu, A. Furusaki, and A. W. W. Ludwig, *Phys. Rev. B* **78**, 195125 (2008).
 - ¹⁰ X.-L. Qi, T. L. Hughes, and S.-C. Zhang, *Phys. Rev. B* **82**, 184516 (2010).
 - ¹¹ M. Sato and Y. Ando, *Reports on Progress in Physics* **80**, 076501 (2017).
 - ¹² X. Wan, A. M. Turner, A. Vishwanath, and S. Y. Savrasov, *Phys. Rev. B* **83**, 205101 (2011).
 - ¹³ A. A. Burkov, *Nature Materials* **15**, 1145 EP (2016).
 - ¹⁴ C. Fang, H. Weng, X. Dai, and Z. Fang, *Chinese Physics B* **25**, 117106 (2016).
 - ¹⁵ H. Wang, J. Ruan, and H. Zhang, *Phys. Rev. B* **99**, 075130 (2019).
 - ¹⁶ B. A. Bernevig and T. L. Hughes, *Topological insulators and topological superconductors* (Princeton university press, 2013).
 - ¹⁷ H. Shen, B. Zhen, and L. Fu, *Phys. Rev. Lett.* **120**, 146402 (2018).
 - ¹⁸ S. Yao and Z. Wang, *Phys. Rev. Lett.* **121**, 086803 (2018).
 - ¹⁹ F. Song, S. Yao, and Z. Wang, *Phys. Rev. Lett.* **123**, 170401 (2019).
 - ²⁰ F. Song, S. Yao, and Z. Wang, *Phys. Rev. Lett.* **123**, 246801 (2019).
 - ²¹ S. Yao, F. Song, and Z. Wang, *Phys. Rev. Lett.* **121**, 136802 (2018).
 - ²² Z. Gong, Y. Ashida, K. Kawabata, K. Takasan, S. Hishikawa, and M. Ueda, *Phys. Rev. X* **8**, 031079 (2018).
 - ²³ N. Okuma, K. Kawabata, K. Shiozaki, and M. Sato, *Phys. Rev. Lett.* **124**, 086801 (2020).
 - ²⁴ F. K. Kunst, E. Edvardsson, J. C. Budich, and E. J. Bergholtz, *Phys. Rev. Lett.* **121**, 026808 (2018).
 - ²⁵ T. Yoshida, K. Kudo, and Y. Hatsugai, *Scientific Reports* **9**, 16895 (2019).
 - ²⁶ F. K. Kunst and V. Dwivedi, *Phys. Rev. B* **99**, 245116 (2019).
 - ²⁷ H. Zhou and J. Y. Lee, *Phys. Rev. B* **99**, 235112 (2019).
 - ²⁸ K. Kawabata, K. Shiozaki, M. Ueda, and M. Sato, *Phys. Rev. X* **9**, 041015 (2019).
 - ²⁹ K. Esaki, M. Sato, K. Hasebe, and M. Kohmoto, *Phys. Rev. B* **84**, 205128 (2011).
 - ³⁰ T. E. Lee, *Phys. Rev. Lett.* **116**, 133903 (2016).
 - ³¹ D. Leykam, K. Y. Bliokh, C. Huang, Y. D. Chong, and F. Nori, *Phys. Rev. Lett.* **118**, 040401 (2017).
 - ³² C. Yin, H. Jiang, L. Li, R. Lü, and S. Chen, *Phys. Rev. A* **97**, 052115 (2018).
 - ³³ A. Cerjan, M. Xiao, L. Yuan, and S. Fan, *Phys. Rev. B* **97**, 075128 (2018).
 - ³⁴ Y. Xu, S.-T. Wang, and L.-M. Duan, *Phys. Rev. Lett.* **118**, 045701 (2017).
 - ³⁵ S. Ke, B. Wang, H. Long, K. Wang, and P. Lu, *Opt. Express* **25**, 11132 (2017).
 - ³⁶ X. Wang, T. Liu, Y. Xiong, and P. Tong, *Phys. Rev. A* **92**, 012116 (2015).
 - ³⁷ C. M. Bender and S. Boettcher, *Phys. Rev. Lett.* **80**, 5243 (1998).
 - ³⁸ I. Rotter, *Journal of Physics A: Mathematical and Theoretical* **42**, 153001 (2009).
 - ³⁹ S. Malzard, C. Poli, and H. Schomerus, *Phys. Rev. Lett.* **115**, 200402 (2015).
 - ⁴⁰ Y. Choi, S. Kang, S. Lim, W. Kim, J.-R. Kim, J.-H. Lee, and K. An, *Phys. Rev. Lett.* **104**, 153601 (2010).
 - ⁴¹ T. E. Lee and C.-K. Chan, *Phys. Rev. X* **4**, 041001 (2014).
 - ⁴² K. G. Makris, R. El-Ganainy, D. N. Christodoulides, and Z. H. Musslimani, *Phys. Rev. Lett.* **100**, 103904 (2008).
 - ⁴³ S. Longhi, *Phys. Rev. Lett.* **103**, 123601 (2009).
 - ⁴⁴ S. Klaiman, U. Günther, and N. Moiseyev, *Phys. Rev. Lett.* **101**, 080402 (2008).
 - ⁴⁵ A. Regensburger, C. Bersch, M.-A. Miri, G. Onishchukov, D. N. Christodoulides, and U. Peschel, *Nature* **488**, 167 (2012).
 - ⁴⁶ S. Bittner, B. Dietz, U. Günther, H. L. Harney, M. Miskioğlu, A. Richter, and F. Schäfer, *Phys. Rev. Lett.* **108**, 024101 (2012).
 - ⁴⁷ C. E. Rüter, K. G. Makris, R. El-Ganainy, D. N. Christodoulides, M. Segev, and D. Kip, *Nature Physics* **6**, 192 (2010).
 - ⁴⁸ Z. Lin, H. Ramezani, T. Eichelkraut, T. Kottos, H. Cao, and D. N. Christodoulides, *Phys. Rev. Lett.* **106**, 213901 (2011).
 - ⁴⁹ L. Feng, Y.-L. Xu, W. S. Fegadolli, M.-H. Lu, J. B. Oliveira, V. R. Almeida, Y.-F. Chen, and A. Scherer, *Nature Materials* **12**, 108 EP (2012).
 - ⁵⁰ A. Guo, G. J. Salamo, D. Duchesne, R. Morandotti, M. Volatier-Ravat, V. Aimez, G. A. Siviloglou, and D. N. Christodoulides, *Phys. Rev. Lett.* **103**, 093902 (2009).
 - ⁵¹ M. Liertzer, L. Ge, A. Cerjan, A. D. Stone, H. E. Türeci, and S. Rotter, *Phys. Rev. Lett.* **108**, 173901 (2012).
 - ⁵² B. Peng, Ş. K. Özdemir, S. Rotter, H. Yilmaz, M. Liertzer, F. Monifi, C. M. Bender, F. Nori, and L. Yang, *Science* **346**, 328 (2014).
 - ⁵³ R. Fleury, D. Sounas, and A. Alù, *Nature Communications* **6**, 5905 (2015).
 - ⁵⁴ L. Chang, X. Jiang, S. Hua, C. Yang, J. Wen, L. Jiang, G. Li, G. Wang, and M. Xiao, *Nature Photonics* **8**, 524 EP (2014).
 - ⁵⁵ H. Hodaei, A. U. Hassan, S. Wittek, H. Garcia-Gracia, R. El-Ganainy, D. N. Christodoulides, and M. Khajavikhan, *Nature* **548**, 187 EP (2017).
 - ⁵⁶ H. Hodaei, M.-A. Miri, M. Heinrich, D. N. Christodoulides, and M. Khajavikhan, *Science* **346**, 975 (2014).
 - ⁵⁷ L. Feng, Z. J. Wong, R.-M. Ma, Y. Wang, and X. Zhang, *Science* **346**, 972 (2014).
 - ⁵⁸ T. Gao, E. Estrecho, K. Y. Bliokh, T. C. H. Liew, M. D.

- Fraser, S. Brodbeck, M. Kamp, C. Schneider, S. Höfling, Y. Yamamoto, F. Nori, Y. S. Kivshar, A. G. Truscott, R. G. Dall, and E. A. Ostrovskaya, *Nature* **526**, 554 EP (2015).
- ⁵⁹ H. Xu, D. Mason, L. Jiang, and J. G. E. Harris, *Nature* **537**, 80 EP (2016).
- ⁶⁰ Y. Ashida, S. Furukawa, and M. Ueda, *Nature Communications* **8**, 15791 (2017).
- ⁶¹ K. Kawabata, Y. Ashida, and M. Ueda, *Phys. Rev. Lett.* **119**, 190401 (2017).
- ⁶² W. Chen, Ş. Kaya Özdemir, G. Zhao, J. Wiersig, and L. Yang, *Nature* **548**, 192 EP (2017).
- ⁶³ K. Ding, G. Ma, M. Xiao, Z. Q. Zhang, and C. T. Chan, *Phys. Rev. X* **6**, 021007 (2016).
- ⁶⁴ C. A. Downing and G. Weick, *Phys. Rev. B* **95**, 125426 (2017).
- ⁶⁵ V. Kozii and L. Fu, (2017), [arXiv:1708.05841](#).
- ⁶⁶ T. Yoshida, R. Peters, and N. Kawakami, *Phys. Rev. B* **98**, 035141 (2018).
- ⁶⁷ K. Kawabata, T. Bessho, and M. Sato, *Phys. Rev. Lett.* **123**, 066405 (2019).
- ⁶⁸ T. Bessho, K. Kawabata, and M. Sato, “Topological classification of non-hermitian gapless phases: Exceptional points and bulk fermi arcs,” (2019), [arXiv:1911.08998 \[cond-mat.mes-hall\]](#).
- ⁶⁹ C.-H. Liu, H. Jiang, and S. Chen, *Phys. Rev. B* **99**, 125103 (2019).
- ⁷⁰ C.-H. Liu and S. Chen, *Phys. Rev. B* **100**, 144106 (2019).
- ⁷¹ T. Yoshida, R. Peters, N. Kawakami, and Y. Hatsugai, *Phys. Rev. B* **99**, 121101 (2019).
- ⁷² D. S. Borgnia, A. J. Kruchkov, and R.-J. Slager, *Phys. Rev. Lett.* **124**, 056802 (2020).
- ⁷³ Z. Yang, C.-K. Chiu, C. Fang, and J. Hu, *Phys. Rev. Lett.* **124**, 186402 (2020).
- ⁷⁴ Z. Yang, A. Schnyder, J. Hu, and C.-K. Chiu, (2019), [arXiv:1912.02788](#).
- ⁷⁵ Y. Xiong, *Journal of Physics Communications* **2**, 035043 (2018).
- ⁷⁶ T. Yoshida, T. Mizoguchi, and Y. Hatsugai, (2019), [arXiv:1912.12022](#).
- ⁷⁷ C. H. Lee and R. Thomale, *Phys. Rev. B* **99**, 201103 (2019).
- ⁷⁸ T. Hofmann, T. Helbig, F. Schindler, N. Salgo, M. Brzezińska, M. Greiter, T. Kiessling, D. Wolf, A. Vollhardt, A. Kabaši, C. H. Lee, A. Bilušić, R. Thomale, and T. Neupert, *Phys. Rev. Research* **2**, 023265 (2020).
- ⁷⁹ Y. Yi and Z. Yang, (2020), [arXiv:2003.02219](#).
- ⁸⁰ K. Zhang, Z. Yang, and C. Fang, (2019), [arXiv:1910.01131](#).
- ⁸¹ K. Yokomizo and S. Murakami, *Phys. Rev. Lett.* **123**, 066404 (2019).
- ⁸² Z. Yang, K. Zhang, C. Fang, and J. Hu, (2019), [arXiv:1912.05499](#).
- ⁸³ J. Carlström and E. J. Bergholtz, *Phys. Rev. A* **98**, 042114 (2018).
- ⁸⁴ T. Yoshida and Y. Hatsugai, *Phys. Rev. B* **100**, 054109 (2019).
- ⁸⁵ C. H. Lee, G. Li, Y. Liu, T. Tai, R. Thomale, and X. Zhang, (2018), [arXiv:1812.02011](#).
- ⁸⁶ L. Li, C. H. Lee, and J. Gong, *Communications Physics* **2**, 135 (2020).
- ⁸⁷ Z. Yang and J. Hu, *Phys. Rev. B* **99**, 081102 (2019).